Experimental observation of ABCB stacked tetralayer graphene

Konstantin G. Wirth,[1,†] Jonas B. Hauck,[2] Alexander Rothstein,[3,4] Dario Siebenkotten,[1] Lennart Klebl,[2] Ammon Fischer,[2] Bernd Beschoten,[3] Christoph Stampfer,[3,4] Lutz Waldecker,[3] Dante M. Kennes,[2,5] and Thomas Taubner[1,‡]

[1] 1^{st} *Institute of Physics, RWTH Aachen University, 52074 Aachen, Germany*
[2] *Institute for Theory of Statistical Physics, RWTH Aachen University, and JARA Fundamentals of Future Information Technology, 52062 Aachen, Germany*
[3] 2^{nd} *Institute of Physics and JARA-FIT, RWTH Aachen University, 52074 Aachen, Germany*
[4] *Peter Grünberg Institute (PGI-9), Forschungszentrum Jülich, 52425 Jülich, Germany*
[5] *Max Planck Institute for the Structure and Dynamics of Matter, Center for Free Electron Laser Science, Hamburg, Germany*

(Dated: March 16, 2022)

In tetralayer graphene, three inequivalent layer stackings should exist, however, only rhombohedral (ABCA) and Bernal (ABAB) stacking have so far been observed. The three stacking sequences differ in their electronic structure, with the elusive third stacking (ABCB) being unique as it is predicted to exhibit an intrinsic bandgap as well as locally flat bands around the K points. Within our random phase approximation, these flat bands are predicted to promote correlated phenomena such as magnetic and unconventional superconducting order. Here, we use scattering-type scanning near-field optical microscopy and confocal Raman microscopy to identify and characterize domains of ABCB stacked tetralayer graphene. We reveal unique optical fingerprints of all three stacking sequences by addressing their infrared conductivities between 0.28 and 0.56 eV using amplitude and phase-resolved near-field nano-spectroscopy. Comparison with results from tight-binding calculations are in good quantitative agreement and allow for unambiguous assignments.

INTRODUCTION

The crystallographic stacking order of few layer graphene (FLG) greatly influences its electronic and optical properties. Naturally occurring crystallographic structures of graphene host interesting phenomena such as quantum Hall states in single and bilayer graphene [1, 2], with Bernal stacked bilayer graphene exhibiting superconductivity upon applying a magnetic field [3].

Half- and quarter-metals have been reported for rhombohedral stacked trilayer graphene [4, 5], while a charge-transfer excitonic insulator and a ferrimagnet are candidates for phases of matter realized in rhombohedral four-layer (ABCA) graphene [6]. In addition, artificial stackings of graphene layers with a twist angle have been shown to lead to flat bands and correlated phenomena [7, 8] such as unconventional superconductivity in twisted bilayer graphene [9] or ferromagnetic insulating states in twisted double bilayer graphene [10, 11].

The most common stacking in FLG is Bernal stacking, which is the energetically favorable configuration [12], while rhombohedral stacking is less common [13, 14]. For tetralayer graphene (4LG), besides rhombohedral and Bernal (ABAB) stackings, also a mixed stacking has been predicted to be metastable, namely the equivalent stackings ABCB and ABAC (here denoted as ABCB) [12, 15], c.f. insets Figure 1 a). This stacking, however, has so far eluded experimental observation.

Here, we provide experimental evidence for ABCB stacked tetralayer graphene by amplitude and phase resolved infrared nano-spectroscopy with scattering-type scanning near-field optical microscopy (s-SNOM). By normalizing the amplitude and phase values to the respective values of ABAB stacking, which is relatively featureless in the investigated energy range, we overcome the issue of the influence of the unknown tip shape on our spectra, and achieve quantitative agreement between measured and calculated amplitude and phase spectra. Furthermore, we employ Raman spectroscopy to reveal the differences in the Raman G, 2D and M peaks between the three stacking orders, which will allow an unambiguous identification of the different domains. This remedies the long-standing elusive nature of the ABCB stacking order and will provide access to intriguing electronic properties, which we predict and investigate within a fluctuation exchange approach. In the following, we review these properties before turning to the experimental results.

LOW-ENERGY ELECTRONIC PROPERTIES

ABCB graphene exhibits a unique electronic band structure [12, 15, 16]: It is the thinnest graphene-based intrinsic band insulator. It has a gap of 8.8 meV [15], which upon application of an out-of-plane electric displacement field should become semi-metallic [12]. In addition, it features strong van-Hove singularities at the band edges. This is shown in Figure 1 a), which displays the low-energy bandstructure, density of states (DOS) and a side view comparing the three crystallographic stackings ABAB, ABCA and ABCB. The electronic structure of ABCB is neither related to the one of Bernal nor to the one of rhombohedral stacked graphene and its low energy spectrum consists of a locally flat (ap-

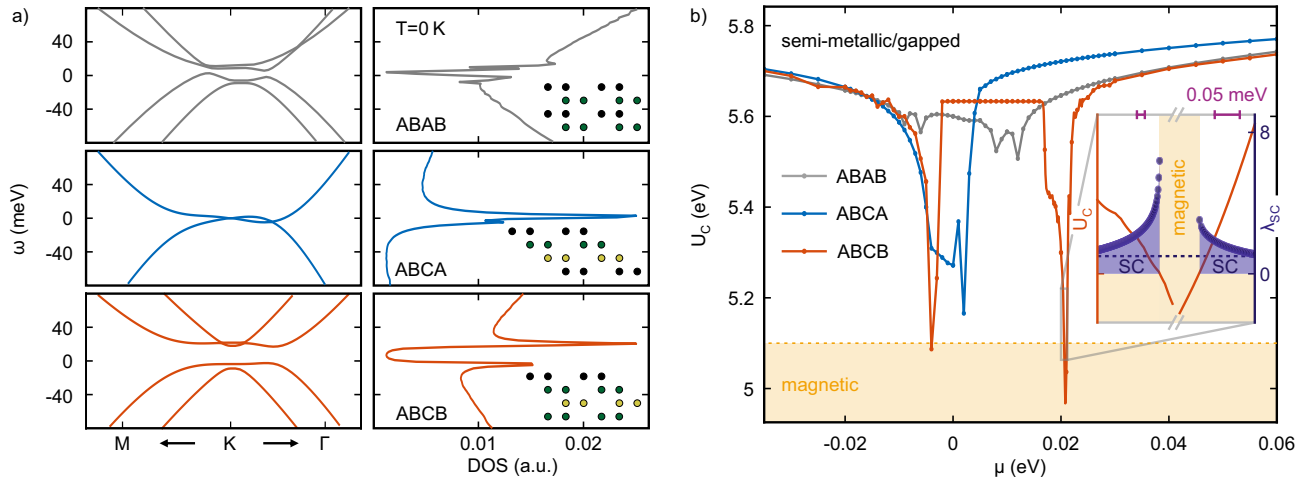

FIG. 1. **Low-energy electronic properties and critical interaction strength for the three 4LG stackings.** a) Low-energy-band structures and density of states (DOS) of tetralayer graphene for three different stacking orders without an applied electric field from the tight-binding model described in the supplementary material section S5. Upper panel ABAB, central panel ABCA and lower panel ABCB. The small insets show the side view of the atomic stackings. Note that the band touching point in ABAB graphene is not correctly captured by this simple model, instead there is still a very small band gap. We introduced an artificial broadening of 1 meV in the calculation. b) Critical interaction strength U_c for magnetic ordering versus chemical potential μ obtained within RPA. Here we chose $U = 5.1\,\text{eV}$ (marked as yellow region in the plot), $T = 10^{-4}\,\text{eV}$ and the low energy models used for panel a). Furthermore, the inset shows the pairing strength λ_{SC}, which is proportional to T_c, to emphasize the emergence of superconductivity within our RPA approach.

proximately cubic) band intersected by a massive Dirac cone [16], promoting the strong van-Hove singularities (vHs) found.

The flat bands (vHs) at the valleys K and K', which emerge in ABCB graphene, render this stacking particularly intriguing from the viewpoint of correlated phenomena. To illustrate this, we study the low-energy phase diagram of ABCB graphene by using a simple Hubbard-type interaction U and employing the random phase approximation (RPA), as outlined in the SI. The resulting critical interaction strength U_c as function of the chemical potential μ is plotted in Figure 1 b) for the three 4LG stackings. The critical interaction strength in ABCB exhibits two pronounced minima according to the RPA at doping levels slightly below $\mu = 0\,\text{eV}$ and close to $\mu = 0.02\,\text{eV}$, corresponding to the valley-flat bands (vHs). This is in accord with a simple generalized Stoner criterion picture. Assuming an interaction of $U = 5.1\,\text{eV}$ [17] in accordance with first principle calculations [18, 19] in graphitic systems, we find that ABCB is the only 4LG configuration in which $U_c < U$ can be fulfilled at values of the chemical potential around that of the vHs. In these regions (where $U_c < U$) the RPA predicts an intriguing magnetic ordering (cf. yellow marked region in Figure 1 b)), while the majority of the phase diagram exhibits paramagnetic behavior ($U_c > U$). Remarkably, although ABCA also exhibits relatively flat bands (vHs) around the high symmetry points, our RPA calculations suggest weaker ordering tendencies in this compound compared to the ABCB stacking. This elevates ABCB stacked 4LG as the most promising platform to study correlation effects.

We furthermore study the possibility of electronic correlation-driven superconductivity in ABCB stacked 4LG (for more details on the calculations and a more in depth analysis of the superconducting order parameters, see SI S5). The inset in Figure 1 b) provides a phase diagram obtained from RPA and FLEX calculations. It shows a zoom around the minimum of the critical interaction strength (red) close to $\mu = 0.02\,\text{eV}$. For $20.4\,\text{meV} \lesssim \mu \lesssim 21.1\,\text{meV}$ (yellow shaded) we find $U_c < U$ and RPA predicts magnetic order. Outside of this region the blue line indicates the strength of the superconducting order parameter λ_{SC}, which is proportional to the critical temperature of the superconducting phase. At chemical potentials close to the magnetic ordering, we find narrow windows that support unconventional f-wave ($l = 3$) superconductivity in the triplet channel, originating from spin- and charge fluctuations of the magnetic parent state. The remarkable low-energy properties of ABCB graphene shown above promise an exciting playground for correlated phenomena in this so far evasive stacking. We now turn to the real-space imaging of stacking orders in 4LG to experimentally unveil ABCB graphene.

DOMAIN IMAGING

To characterize different graphene stacking orders, optical techniques offer a wide range of tools. Absorption measurements in the infrared regime between 0.2 and 0.9 eV of FLG give access to characteristic absorption peaks around the interband transitions, which can be directly linked to the electronic structure [20], and have thus been used to distinguish ABCA and ABAB [21] stacked 4LG. Confocal Raman spectroscopy is another tool for identifying stacking orders in FLG [22], though both methods are limited in spatial resolution by diffraction. Thus, common far-field spectroscopy methods are prone to overlook small domains on these flakes, in particular those of unknown crystallographic stackings.

The diffraction limit can be overcome by employing infrared scattering type scanning near-field optical microscopy (s-SNOM), which enables infrared nano-imaging with a lateral resolution down to 20 nm [23]. s-SNOM enabled the real-space observation of surface plasmon polaritons (SPPs) in graphene [24, 25]. With the help of SPP reflection at inhomogeneities, s-SNOM has also been used to image grain boundaries [26], and solitons in FLG [27–29] as well as twisted bilayer graphene [30] and other moiré heterostructures [31]. At photon energies above 0.2 eV, s-SNOM gives access to the stacking-specific optical conductivities of FLG, and the scattering amplitude and phase values can be retrieved simultaneously. This allows to assign sub-diffraction FLG domains to stackings by recording images at specific photon energies [32, 33]. Recently, it has been shown for IR nano-spectroscopy on bilayer graphene around the conductivity resonances at 0.39 eV that optical amplitude and phase scale with the characteristics of real and imaginary part of the conductivity [34]. However, the quantitative agreement between theoretical prediction and experimental data in these studies is still lacking.

Figure 2 a) shows the schematic of a scattering-type scanning near field optical microscope used to investigate the stacking order of 4LG flakes. Infrared light from a broadly tunable laser source is focused onto an atomic force microscope tip operated in tapping mode. From the back-scattered light, near-field signals at higher harmonics of the probe's tapping frequency are obtained. Here, we show third order optical amplitude (S_3) and phase (Φ_3) signals, which are recorded simultaneously to the topography (see Methods) [35].

In Figure 2 b), the topography of a scanned 4LG flake (Flake 1) is shown. It reveals two segments of 4LG separated by a small stripe of trilayer graphene (TLG). Except for two diagonal folds, the 4LG is mostly homogeneous. The simultaneously recorded optical amplitude (S_3) and phase images (Φ_3) in Figures 2 c) and e) are obtained at photon energies of 0.34 eV. In these images, the FLG flake can be clearly distinguished from the SiO_2 substrate.

In the large 4LG segment, distinct amplitude and phase values are present in differently sized domains across the flake. The amplitude $\tilde{S}$=$S_3/S_3(SiO_2)$ and phase $\tilde{\Phi}_3 = \Phi_3$-$\Phi_3(SiO_2)$ contrasts extracted from the 4LG area, referenced to the adjacent SiO_2, are shown in a polar plot in Figure 2 d). Whereas pixel-to-pixel fluctuations are relatively large, three distinct clusters of different amplitude and phase response are identified. The different near-field responses originate from different optical conductivities across the 4LG, which the s-SNOM is sensitive to [32, 34]. As the conductivities are connected to the electronic structure, we associate the distinct near-field responses with the three crystallographic stackings of 4LG [21] (ABAB, ABCA and ABCB).

The stacking assignment is supported by the different spectroscopic response at various infrared photon energies, which is also used to assign the domains in Figures 2 c)-f), and is discussed further in the text. Further evidence comes from confocal Raman spectroscopy of the few layer graphene Raman G, M, and 2D peaks. A Raman map of the G peak position is shown in Figure 2 f). The largest domains of each stacking sequence, as identified in the s-SNOM amplitude and phase images by the labels, similarly show three distinct peak positions. However, some smaller domains observed in Figure 2 c) and e) cannot be fully resolved in the Raman map due to the diffraction limit.

We now turn to the characterization of the ABCB domains and discuss its fingerprints in Raman spectroscopy as well as in its infrared optical response.

RAMAN SPECTRA

Raman spectra of the G and 2D peak of the three stacking orders are shown in Figures 3 a) and b), respectively (M peaks in the inset). Within individual samples, the G peak position and width show small changes between different domains, even though their absolute values depend on strain and doping [36, 37] and vary between samples. We observe the G-peak position of ABCA stacking to be red-shifted compared to ABAB, which is consistent with the shift observed in ABC and ABA stacked trilayer graphene [14]. For ABCB domains, we find the G peak to be at slightly higher energies compared to both other stackings. Notably, the full width at half maximum (FWHM) linewidth of the G peak is the smallest in the ABCA domains and largest in the ABAB domains.

The 2D and M peaks both originate from two-phonon processes and are thus sensitive to the electronic structure as well [38–40]. As a result, both peaks show distinct line shapes for all three stacking orders. Compared to the ABAB 2D peak, which is quite symmetric and featureless, the ABCA 2D peak shows a stronger asymmetry, a

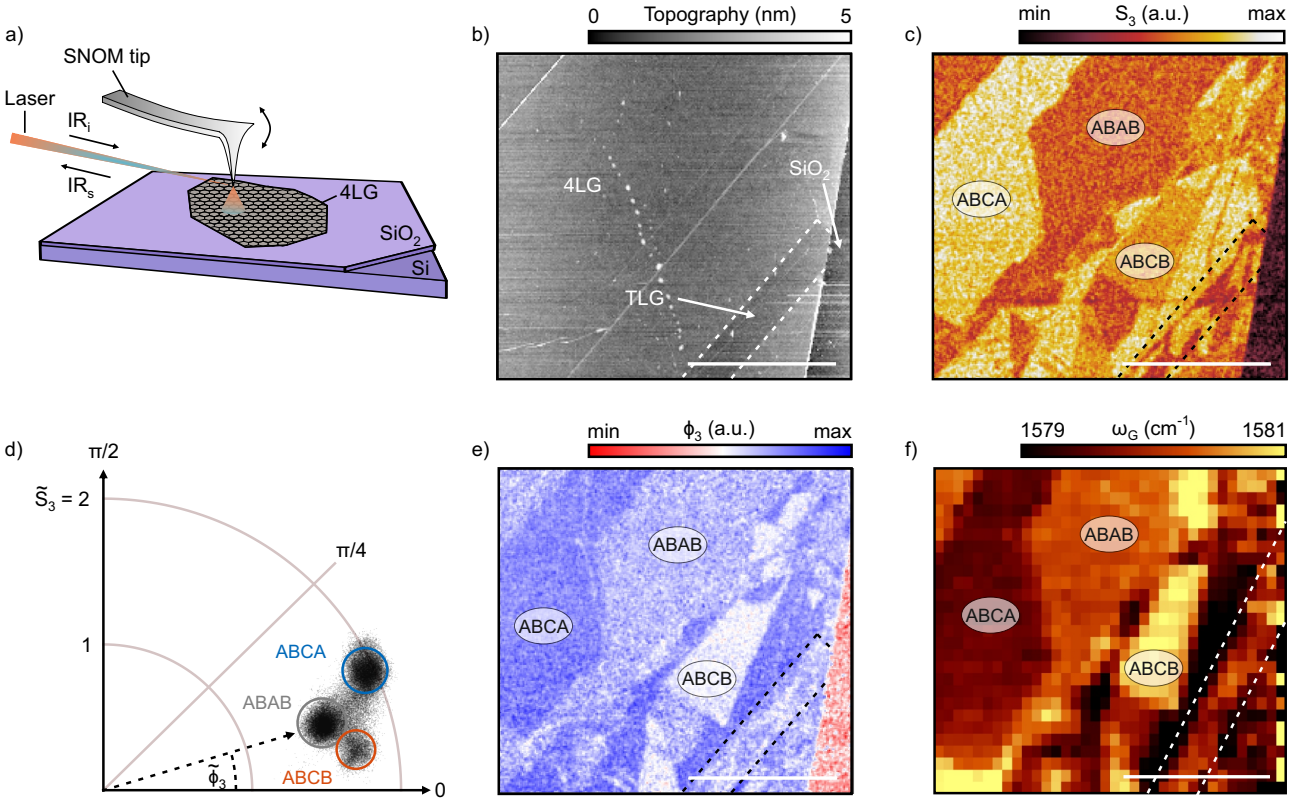

FIG. 2. **Optical investigation of a 4LG flake.** a) Schematic of the s-SNOM set up with an infrared laser focused on the apex of the atomic force microscope tip. b) Topography image of a 4LG flake on SiO_2. c), e) Corresponding optical amplitude (S_3) and phase (Φ_3) images revealing domains of different s-SNOM signal, obtained at 0.34 eV. Three domains on the 4LG with different amplitude values are indicated by ABCB, ABCA and ABAB. The dashed rectangle marks the position of the TLG (compare with b)). d) Scatter plot of normalized amplitude ($\tilde{S} = S_3/S_3(SiO_2)$) and phase ($\tilde{\Phi}_3 = \Phi_3 - \Phi_3(SiO_2)$) of individual pixels obtained at 0.34 eV on the 4LG plotted in a polar plot and referenced to the SiO_2. The circles are a guide to the eye to identify the respective domains. f) Raman map of the G peak position. The three different domains marked in c) can also be identified. The dashed lines mark the border between 4LG and TLG (see panel b)). The scale bars corresponds to 5 µm.

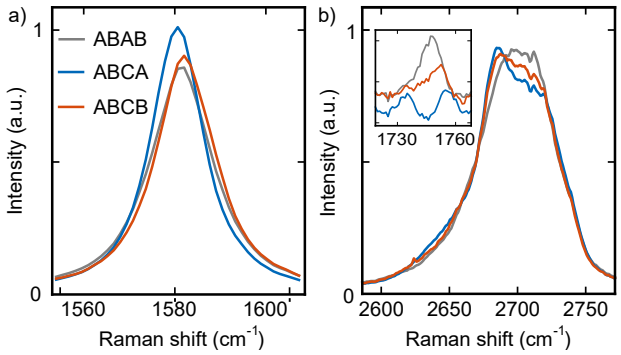

FIG. 3. **Raman spectroscopy of the 4LG stackings.** Raman spectra of a) the G peaks and b) the 2D peaks of the three stacking orders (normalized by their total intensity). The inset in b) shows the M peaks.

sharp feature around 2680 cm^{-1} and a shoulder around 2640 cm^{-1}. These signatures are consistent with previously reported Raman spectra [14, 40–42]. The ABCB 2D peak appears like an interpolation of the two other peaks: it is more asymmetric than the ABAB peak, but shows a less pronounced feature on the low-energy side compared to the ABCA peak and no low-energy shoulder. The M-peaks [39] show a unique peak shape and position for each stacking, but might be impractical for rapid domain identification due to their comparably low intensity. The Raman spectra confirm the domain assignment by our s-SNOM measurements. A detailed theoretical study of the Raman G- and M-peaks of ABCB is beyond the scope of this paper.

OPTICAL CONDUCTIVITY

To characterize the different optical conductivities following from the electronic structures, sequential nanospectroscopy between 0.28 eV and 0.56 eV in conjunction with theoretical modelling was conducted. Figure 4

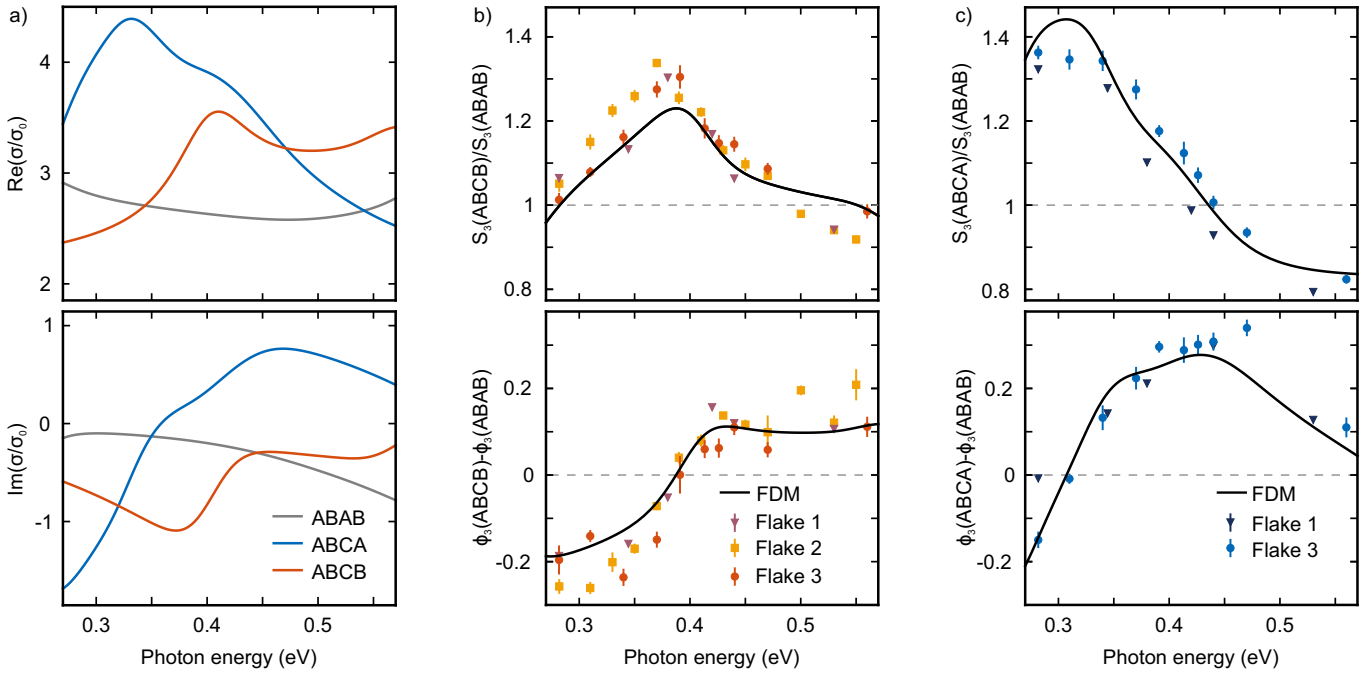

FIG. 4. **s-SNOM nano-spectroscopy of 4LG stackings**. a) Real- and imaginary part of the optical conductivity of the three different stacking orders obtained from tight binding calculations of 4LG for $\mu = 50$ meV with a phenomenologically chosen broadening of $\eta = 40$ meV. b) Third demodulation order amplitude S_3 (top) and phase Φ_3 (bottom) data compared to theoretical s-SNOM spectra of ABCB referenced to ABAB for three different flakes. c) Third demodulation order amplitude (top) and phase (bottom) data compared to theoretical spectra for ABCA referenced to ABAB. Images of Flake 1 and Flake 2 can be found in the SI. The theoretical spectra are obtained from finite dipole model calculations.

a) shows the optical conductivities σ of the three crystallographic stackings ABAB, ABCA and ABCB. The optical conductivities are obtained from tight binding calculations including nearest-neighbor interlayer- and nearest-neighbor intralayer hopping with hopping energies of $\gamma_{\text{inter}} = 0.39\,\text{eV}$ and $\gamma_{\text{intra}} = 3.16\,\text{eV}$, respectively (see SI S4). Note that this Hamiltonian, while being simpler compared to the one used for the calculation in Figure 1, is optimized to reproduce the band structure at the comparably higher energies of the s-SNOM measurements [12, 21]. The chemical potential ($\mu = 50$ meV) and a phenomenological broadening ($\eta = 40$ meV) are chosen to achieve a good match with the s-SNOM data of Flake 3 (see SI S3).

Real- and imaginary part of the conductivity of ABAB are featureless and almost flat between 0.28 and 0.56 eV. Accordingly, we expect a homogeneous amplitude (S_3) and phase (Φ_3) response for ABAB when compared to ABCA and ABCB, because these reproduce the characteristic features of real and imaginary part of the conductivity [34].

In total, three different 4LG flakes showing three different domains at 0.34 eV were investigated (Flake 1 in Figure 2; Flake 2 and Flake 3 in SI S1). The amplitude and phase contrasts are evaluated line-wise, because of a phase drift, and referenced to the adjacent ABAB values. This referencing overcomes the strong tip dependence of the s-SNOM response of these thin films and makes the results from the three flakes quantitatively comparable.

Amplitude and phase spectra of ABCB- and ABCA-domains, referenced to the ABAB-domains, are shown in Figures 4 b) and c). Note, that Flake 1, 2 and 3 refer to three independently investigated 4LG flakes (see SI S1). The theoretical spectra were obtained from the optical conductivities using a multilayer extension of the finite-dipole model (FDM) [43], in which the graphene layers are taken into account as infinitesimal thin interfaces with a conductivity obtained from tight binding calculations (for Details see SI S2). Both, amplitude and phase data reproduce the characteristics of the calculated s-SNOM contrast well, constituting our assignment of the domains in Figure 2 c).

The normalized amplitude data sets $S_3(\text{ABCB})/S_3(\text{ABAB})$ exhibit a peak at 0.38 eV. The corresponding phase contrast $\Phi_3(\text{ABCB})$-$\Phi_3(\text{ABAB})$ increases with photon energy and has a zero crossing around 0.4 eV. For comparison, amplitude and phase contrast data of domain ABCA are plotted in Figure 4 c). Similar domains were investigated on two of the three flakes. The spectral ABCA data in amplitude and phase are clearly distinct from the response of ABCB: at low energies down to 0.28 eV the amplitude

contrast is much larger than in b) while above, it is monotonically decreasing with photon energy to values below one above 0.45 eV. The experimental data for both stackings, referenced to ABAB, quantitatively match the calculation at almost all measured photon energies. This shows that the optical response in the entire IR region from 0.28 eV to 0.56 eV can be used to distinguish the three stacking orders. Thus, the detection of ABCB domains in s-SNOM is not restricted to our set-up employing a tunable laser source, but could also be achieved with a more commonly available Helium-Neon laser, which can be operated at 0.366 eV, and has been used to distinguish between TLG and FLG stackings in s-SNOM [32].

ABUNDANCE AND STABILITY OF ABCB DOMAINS

Theoretical calculations suggest that ABCB domains are metastable at a higher total energy than ABAB and ABCA [12], whereas in published experimental work, the stacking had so far not been observed. In total, we have scanned an area of 5000 µm^2 of exfoliated tetralayer graphene and found ABCB domains to make up approximately 0.5% of the total area (ABAB to ABCA were around 81.5% and 18.5%, respectively). The largest domain was approximately 10 µm^2 in size. This might explain why, so far, these domains have been overlooked in published work. We note, that on two of the three flakes investigated in this study, ABCB domains appeared at the sample edges. The ABCB domains were stable over the course of several weeks at ambient conditions as well as when subjected to s-SNOM and Raman measurements at moderate laser powers. At higher laser power, we observed the shrinkage of domains (for details see SI S1) which has also been observed for metastable rhombohedral TLG [13].

DISCUSSION

Our experimental results reveal the existence of ABCB stacked tetralayer graphene domains. This observation is enabled by addressing the low-energy electronic structure through the optical conductivity with a tunable laser between 0.28 and 0.56 eV in an s-SNOM setup. The optical conductivity has unique fingerprints for each stacking which manifests themselves in peaks in the normalized scattering amplitude and phase spectra. These features show a broadening of approximately 40 meV, which is below reported values of 50 meV in comparable FTIR studies [20]. Encapsulation in hBN and experiments at lower temperature might further decrease the broadening and allow for spectroscopic measurements with higher energy resolution. Our advanced s-SNOM methods, which go beyond the state of the art Raman technology shows that s-SNOM is not only capable of distinguishing, but also of characterizing stacking orders in FLG through nano-spectroscopy. These findings will ultimately enable the selection of distinct regions for fabricating transport devices.

From the stability and abundance of our measured samples, we conclude that ABCB domains are metastable at room temperature, however, the least abundant occurring domains after tape exfoliation. This agrees with theoretical predictions where the energy barrier between ABCB and ABAB is expected to be lower when compared to ABCA and ABCB [12].

The new stacking is of high interest, because it is the thinnest naturally occurring FLG stacking with an intrinsic bandgap [12, 15, 16] and its low energy physics is dominated by valley flat bands promoting the effect of electron interactions. To this end, our theoretical calculations elevate ABCB graphene over the related ABCA and ABAB stackings as it exhibits stronger tendency towards magnetic ordering and potentially realizes an unconventional f-wave triplet superconductor for certain filling ranges. This is particularly interesting given the recent observation of possible triplet superconductivity in twisted multilayer graphene systems [44, 45] as well as in Bernal stacked graphene [3] and ABC trilayer graphene [4], where regions of zero resistance remain under the presence of strong magnetic fields and large Pauli-limit violations are observed. Going beyond, future theoretical studies of the effects of longer ranged interactions as well as the inclusion of phonons are pressing issues. Furthermore, playing to the unique intrinsic narrow band-gap insulating behavior of ABCB graphene, one faces the natural question whether excitonic physics might play a prominent role as well. Studying these questions is an intriguing avenue of future research.

METHODS

Exfoliation Exfoliation is performed on commercially available silicon wafers with an oxide thickness of 90 nm. Suitable flakes were identified via their optical contrast using a standard optical microscope.

s-SNOM We use a commercially available s-SNOM (NeaSNOM, neaspec GmbH) at photon energies between 0.28 to 0.56 eV for sequential nano-spectroscopy on 4LG in combination with a LN2 cooled InSb detector (Infrared Associates). The s-SNOM is operated in pseudo-heterodyne detection mode, to record amplitude and phase simultaneously. The laser source is a commercially available tunable OPO/OPA laser system (Alpha Module, Stuttgart Instruments) with an energy resolution of 6 meV, which can address the energy range from 0.27 to 0.9 eV. The laser source emits pulses with a pulse length of 1 ps and has a repetition rate of 42 MHz. The s-SNOM

is operated at tapping frequencies of 220-270 kHz at tapping amplitudes of 50-60 nm. We extracted the signal from the third demodulation order amplitude and phase. For single imaging with s-SNOM in pseudo-heterodyne detection mode, this pulse width is sufficient in the investigated energy range as recently shown [34, 46].

Raman spectroscopy Raman maps were taken using a 532 nm laser focused down to a spotsize of approximately 500 nm. The Raman spectra shown in Figure 4, were obtained by averaging the Raman maps within the individual stacking domains. The excitation power was mostly kept to 1.5 mW or below, as higher laser powers occasionally resulted in shrinkage of ABCA and ABCB domains.

Theory We use an in-house hybrid CPU/GPU architecture implementation for the random phase approximation calculations. The calculations were performed for a regular 24×24 bosonic mesh, whereas the integration mesh was chosen to 4800×4800 in order to resolve all low energy features. More details of the implementation can be found in SI 5.

ACKNOWLEDGEMENTS

This work was supported by the Excellence Initiative of the German federal and state governments, the Ministry of Innovation of North Rhine-Westphalia and the Deutsche Forschungsgemeinschaft. KGW, DS and TT acknowledge support from the Deutsche Forschungsgemeinschaft (DFG) within the collaborative research center SFB 917 and within Grant Agreement No. TA 848/7-1. AR, BB, CS, and LW acknowledge support from the European Union's Horizon 2020 research and innovation programme under grant agreement No. 881603 (Graphene Flagship), the Deutsche Forschungsgemeinschaft (DFG, German Research Foundation) under Germany's Excellence Strategy - Cluster of Excellence Matter and Light for Quantum Computing (ML4Q) EXC 2004/1 - 390534769, through DFG (BE 2441/9-1), and the FLAG-ERA grant TATTOOS, by the Deutsche Forschungsgemeinschaft (DFG, German Research Foundation) - 437214324. JBH, LK, AF and DMK acknowledge funding by the Deutsche Forschungsgemeinschaft (DFG, German Research Foundation) under RTG 1995, within the Priority Program SPP 2244 "2DMP" and under Germany's Excellence Strategy - Cluster of Excellence Matter and Light for Quantum Computing (ML4Q) EXC 2004/1 - 390534769. DMK acknowledges support by the Max Planck-New York City Center for Nonequilibrium Quantum Phenomena. We acknowledge computational resources provided by the Max Planck Computing and Data Facility and RWTH Aachen University under project number rwth0742 and rwth0716.

AUTHOR CONTRIBUTIONS

KGW, JBH, LW, DMK, BB, CS and TT conceived the project. AR fabricated the samples. KGW and DS performed the s-SNOM experiments and theoretical contrast calculations. AR and LW carried out the Raman measurements. LW and KGW analysed the experimental data. JBH carried out the theoretical calculation of the band structure and optical conductivity. LK performed the RPA calculations. AF perfomed the linearized gap calculations. All authors contributed to writing the manuscript.

COMPETING INTERESTS

The authors declare no competing interests.

† konstantin.wirth@rwth-aachen.de
‡ taubner@physik.rwth-aachen.de

[1] Zhang, Y., Tan, Y.-W., Stormer, H. L. & Kim, P. Experimental observation of the quantum Hall effect and Berry's phase in graphene. *Nature* **438**, 201–204 (2005).
[2] Novoselov, K. S. *et al.* Unconventional quantum Hall effect and Berry's phase of 2π in bilayer graphene. *Nat. Phys.* **2**, 177–180 (2006).
[3] Zhou, H. *et al.* Isospin magnetism and spin-triplet superconductivity in Bernal bilayer graphene. *arXiv:2110.11317 [cond-mat]* (2021).
[4] Zhou, H., Xie, T., Taniguchi, T., Watanabe, K. & Young, A. F. Superconductivity in rhombohedral trilayer graphene. *Nature* **598**, 434–438 (2021).
[5] Zhou, H. *et al.* Half- and quarter-metals in rhombohedral trilayer graphene. *Nature* **598**, 429–433 (2021).
[6] Kerelsky, A. *et al.* Moiréless correlations in ABCA graphene. *Proceedings of the National Academy of Sciences* **118**, e2017366118 (2021).
[7] Balents, L., Dean, C. R., Efetov, D. K. & Young, A. F. Superconductivity and strong correlations in moiré flat bands. *Nature Physics* **16**, 725–733 (2020).
[8] Kennes, D. M. *et al.* Moiré heterostructures as a condensed-matter quantum simulator. *Nature Physics* **17**, 155–163 (2021).
[9] Cao, Y. *et al.* Unconventional superconductivity in magic-angle graphene superlattices. *Nature* **556**, 43–50 (2018).
[10] Liu, X. *et al.* Tunable spin-polarized correlated states in twisted double bilayer graphene. *Nature* **583**, 221–225 (2020).
[11] Shen, C. *et al.* Correlated states in twisted double bilayer graphene. *Nature Physics* **16**, 520–525 (2020).
[12] Aoki, M. & Amawashi, H. Dependence of band structures on stacking and field in layered graphene. *Solid State Communications* **142**, 123–127 (2007).
[13] Zhang, J. *et al.* Light-induced irreversible structural phase transition in trilayer graphene. *Light: Science & Applications* **9**, 174 (2020).

[14] Lui, C. H. *et al.* Imaging Stacking Order in Few-Layer Graphene. *Nano Letters* **11**, 164–169 (2011).

[15] Latil, S. & Henrard, L. Charge Carriers in Few-Layer Graphene Films. *Physical Review Letters* **97**, 036803 (2006).

[16] Min, H. & MacDonald, A. H. Electronic Structure of Multilayer Graphene. *Progress of Theoretical Physics Supplement* **176**, 227–252 (2008).

[17] Goodwin, Z. A. H. *et al.* Flat bands, electron interactions, and magnetic order in magic-angle mono-trilayer graphene. *Physical Review Materials* **5** (2021).

[18] Wehling, T. O. *et al.* Strength of effective coulomb interactions in graphene and graphite. *Phys. Rev. Lett.* **106**, 236805 (2011).

[19] Schüler, M., Rösner, M., Wehling, T. O., Lichtenstein, A. I. & Katsnelson, M. I. Optimal hubbard models for materials with nonlocal coulomb interactions: Graphene, silicene, and benzene. *Phys. Rev. Lett.* **111**, 036601 (2013).

[20] Mak, K. F., Sfeir, M. Y., Misewich, J. A. & Heinz, T. F. The evolution of electronic structure in few-layer graphene revealed by optical spectroscopy. *Proceedings of the National Academy of Sciences* **107**, 14999–15004 (2010).

[21] Mak, K. F., Shan, J. & Heinz, T. F. Electronic Structure of Few-Layer Graphene: Experimental Demonstration of Strong Dependence on Stacking Sequence. *Physical Review Letters* **104**, 176404 (2010).

[22] Lui, C. H., Li, Z., Mak, K. F., Cappelluti, E. & Heinz, T. F. Observation of an electrically tunable band gap in trilayer graphene. *Nature Physics* **7**, 944–947 (2011).

[23] Taubner, T., Hillenbrand, R. & Keilmann, F. Performance of visible and mid-infrared scattering-type near-field optical microscopes. *Journal of Microscopy* **210**, 311–314 (2003).

[24] Fei, Z. *et al.* Gate-tuning of graphene plasmons revealed by infrared nano-imaging. *Nature* **487**, 82–85 (2012).

[25] Chen, J. *et al.* Optical nano-imaging of gate-tunable graphene plasmons. *Nature* **487**, 77–81 (2012).

[26] Fei, Z. *et al.* Electronic and plasmonic phenomena at graphene grain boundaries. *Nature Nanotechnology* **8**, 821–825 (2013).

[27] Jiang, L. *et al.* Soliton-dependent plasmon reflection at bilayer graphene domain walls. *Nature Materials* **15**, 840–844 (2016).

[28] Jiang, B.-Y. *et al.* Plasmon Reflections by Topological Electronic Boundaries in Bilayer Graphene. *Nano Letters* **17**, 7080–7085 (2017).

[29] Jiang, L. *et al.* Manipulation of domain-wall solitons in bi- and trilayer graphene. *Nature Nanotechnology* **13**, 204–208 (2018).

[30] Sunku, S. S. *et al.* Photonic crystals for nano-light in moiré graphene superlattices. *Science* **362**, 1153–1156 (2018).

[31] Halbertal, D. *et al.* Moiré metrology of energy landscapes in van der waals heterostructures. *Nature Communications* **12** (2021).

[32] Kim, D.-S. *et al.* Stacking Structures of Few-Layer Graphene Revealed by Phase-Sensitive Infrared Nanoscopy. *ACS Nano* **9**, 6765–6773 (2015).

[33] Jeong, G. *et al.* Mapping of Bernal and non-Bernal stacking domains in bilayer graphene using infrared nanoscopy. *Nanoscale* **9**, 4191–4195 (2017).

[34] Wirth, K. G. *et al.* Tunable s-SNOM for Nanoscale Infrared Optical Measurement of Electronic Properties of Bilayer Graphene. *ACS Photonics* **8**, 418–423 (2021).

[35] Keilmann, F. & Hillenbrand, R. Near-field microscopy by elastic light scattering from a tip. *Philosophical Transactions of the Royal Society of London. Series A: Mathematical, Physical and Engineering Sciences* **362**, 787–805 (2004).

[36] Toporski, J., Dieing, T. & Hollricher, O. (eds.) *Confocal Raman Microscopy*, vol. 66 of *Springer Series in Surface Sciences* (Springer International Publishing, Cham, 2018).

[37] Neumann, C. *et al.* Raman spectroscopy as probe of nanometre-scale strain variations in graphene. *Nat. Commun.* **6**, 1–7 (2015).

[38] Malard, L., Pimenta, M., Dresselhaus, G. & Dresselhaus, M. Raman spectroscopy in graphene. *Physics Reports* **473**, 51–87 (2009).

[39] Cong, C., Yu, T., Saito, R., Dresselhaus, G. F. & Dresselhaus, M. S. Second-order overtone and combination raman modes of graphene layers in the range of 1690-2150 cm-1. *ACS Nano* **5**, 1600–1605 (2011).

[40] Torche, A., Mauri, F., Charlier, J.-C. & Calandra, M. First-principles determination of the Raman fingerprint of rhombohedral graphite. *Physical Review Materials* **1**, 041001 (2017).

[41] Nguyen, T. A., Lee, J.-U., Yoon, D. & Cheong, H. Excitation energy dependent Raman signatures of ABA- and ABC-stacked few-layer graphene. *Scientific Reports* **4**, 4630 (2014).

[42] Geisenhof, F. R. *et al.* Anisotropic Strain-Induced Soliton Movement Changes Stacking Order and Band Structure of Graphene Multilayers: Implications for Charge Transport. *ACS Applied Nano Materials* **2**, 6067–6075 (2019).

[43] Hauer, B., Engelhardt, A. P. & Taubner, T. Quasi-analytical model for scattering infrared near-field microscopy on layered systems. *Optics Express* **20**, 13173–13188 (2012).

[44] Zhang, Y. *et al.* Ascendance of superconductivity in magic-angle graphene multilayers. *arXiv:2112.09270 [cond-mat]* (2021).

[45] Park, J. M. *et al.* Magic-angle multilayer graphene: A robust family of moiré superconductors. *arXiv:2112.10760 [cond-mat]* (2021).

[46] Lu, J. *et al.* Observing 0D subwavelength-localized modes at ˜100 THz protected by weak topology. *Science Advances* **7**, eabl3903 (2021).

[47] Cvitkovic, A., Ocelic, N. & Hillenbrand, R. Analytical model for quantitative prediction of material contrasts in scattering-type near-field optical microscopy. *Optics Express* **15**, 8550 (2007).

[48] Zhan, T., Shi, X., Dai, Y., Liu, X. & Zi, J. Transfer matrix method for optics in graphene layers. *Journal of Physics: Condensed Matter* **25**, 215301 (2013).

[49] Kubo, R. Statistical-Mechanical Theory of Irreversible Processes. I. General Theory and Simple Applications to Magnetic and Conduction Problems. *Journal of the Physical Society of Japan* **12**, 570–586 (1957). _eprint: https://doi.org/10.1143/JPSJ.12.570.

[50] Grüneis, A. *et al.* Tight-binding description of the quasiparticle dispersion of graphite and few-layer graphene. *Phys. Rev. B* **78**, 205425 (2008).

Supplementary material: Experimental observation of ABCB stacked tetralayer graphene

S1 Stability and abundance

In Figure S1 the optical phase (Φ_3) and a Raman map of the 4LG flake labeled Flake 2 in the main text are shown over the course of several measurements. The phase image (Φ_3) in Figure S1 a) is recorded at a photon energy of 0.34 eV. The 4LG flake can be clearly distinguished from the SiO_2 substrate on the left (red area). Three regions on the 4LG are marked with their respective stacking. The domain with the weakest contrast towards the SiO_2 is ABCB and the strongest ABCA.

The Raman map around the 2D peak recorded after the s-SNOM measurements is depicted in Figure S1 b). The ABCA-domain is shrunken in the middle of the image, while the ABCB-domain is still present. However, due to the limited resolution of the Raman, the exact shape of the domains is difficult to determine. Subsequent s-SNOM measurements repeated at 0.34 eV are depicted in Figure S1 c). The ABCA-domain has a similar size to what can be expected from the Raman in Figure S1 b), while the ABCB-domain shrunk again to a small stripe and a triangluar feature at the right side of the image. This feature is indicated by a black dashed rectangle, which corresponds to the region investigated with IR nano-spectroscopy. In Figure S1 d) Raman spectra around the 2D peak corresponding to the map in Figure S1 b) are shown. The different domains exhibit similar features like in Figure 3 b).

In Figure S2 a) the topography of the 4LG flake labeled as Flake 3 in the main text is shown. The topography image of the 4LG is featureless, only a few dirt particles and the SiO_2 substrate can be identified, indicating a homogenous number of four graphene layers.

In the corresponding optical amplitude (S_3) and phase image (Φ_3) in Figure S2 b) and c) recorded at a photon energy of 0.34 eV the flake can be clearly distinguished from the SiO_2 substrate. It shows three different amplitude and phase signals on the topographically featureless 4LG. The corresponding domains are indicated by ABAB, ABCA and ABCB. ABAB-domains cover the largest part of the 4LG . Two small domains of the largest contrast correspond to ABCA stacking. The triangular shaped ABCB-domain is located at the edge between 4LG and the SiO_2 and has an amplitude signal between those of ABAB- and ABCA-domain. In the phase image in Figure S2 c) the same three domains can be identified. Again, the phase response is the largest with respect to the SiO_2 for the ABCA-domain and weakest for ABCB.

During our investigations, the domains of Flake 1 (main text) remained stable over several s-SNOM and Raman measurements (over the course of several weeks). For Flake 2 shown in Figure S1, however, we observed the consecutive collapse of a large ABCB domain to a small triangular shaped domains after Raman mapping at laser powers in the range of 3 mW. Such a change in the stacking order has been reported for TLG [S13], albeit for significantly higher laser power. The third investigated flake (Flake 3, Figure S2) also shows a triangular shaped similar sized domain of ABCB stacking, possibly a remnant of a collapsed larger domain. This argument is supported by investigations of the respective area with s-SNOM at a wavelength of 10.6 µm (Figure S2 d)), which reveals a small boundary like feature, indicated by the black box, similar to a shear soliton observed in bilayer graphene [S27] and TLG [S29]. The energy barrier between ABCB and ABAB stacking is expected to be much lower compared to the transition from ABCA to ABAB [S12]. This instability might hamper device fabrication, because the ABCB stacking can transform to energetically favorable Bernal stacking, similar to metastable rhombohedral graphene upon stress or strain during device fabrication [S42].

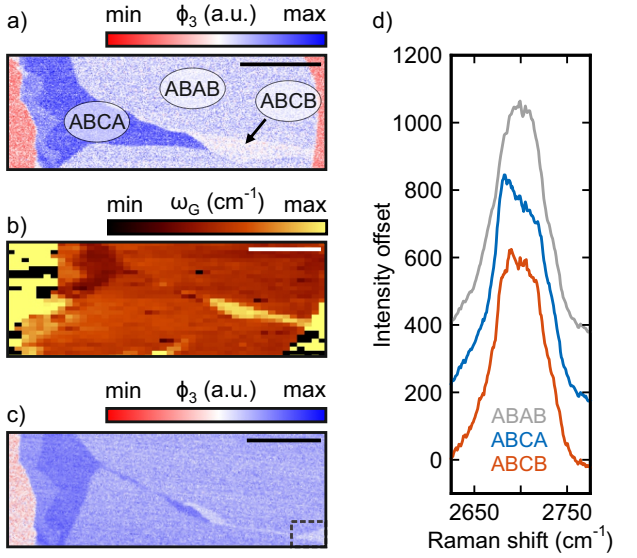

FIG. S1. Flake 2: a) Optical phase (Φ_3) image of a 4LG flake on SiO_2, recorded first at 0.34 eV. b) Raman map around the 2D peak, recorded after the s-SNOM measurement with a high intensity Raman laser reveal a shrinkage of ABCA domain. c) Subsequent optical phase (Φ_3) image obtained at photon energies of 0.34 eV, after the Raman measurements, reveal a shrinkage of the ABCB domain when compared to b) and a). The dashed box indicates the region where s-SNOM nano-spectroscopy was conducted. d) Raman spectra recorded in the different regions for the three domains in b). The scalebars correspond to 5 µm each.

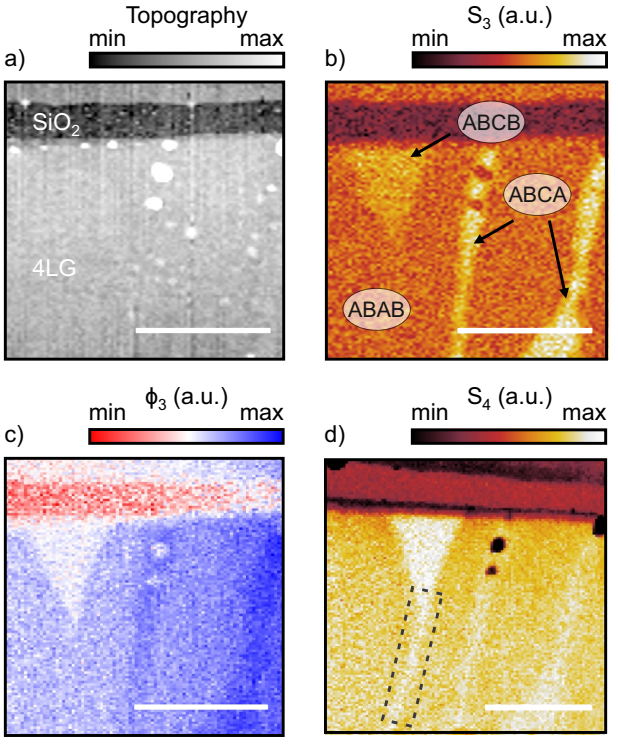

FIG. S2. Flake 3: a) Topography image of the 4LG-only flake on SiO_2. b), c) Corresponding optical amplitude (S_3) and phase (Φ_3) images obtained at photon energies of 0.34 eV, revealing regions of different s-SNOM signal, with three different domains indicated by ABAB, ABCA and ABCB. The domains correspond to the same domains as in Figure 2 of the main text. d) Amplitude image obtained at 10.6 µm of the same area. A bright line below the ABCB domain is visible. The scale bar corresponds to 1 µm.

S2 s-SNOM Contrast calculation

The s-SNOM contrast for the 4LG/SiO2/Si layer stack is calculated with the finite dipole model [S47] with an extension for layered samples [S43] as described in [S34].

The effective polarizability of the tip-sample system is calculated via

$$\alpha_{\text{eff}} = W_0^2 L \frac{\frac{2L}{a} + \ln\frac{a}{4eL}}{\ln\frac{4L}{e^2 a}}(2 + \eta_r(z)) \tag{S1}$$

where a is the tip radius, L is the effective length of the assumed sphere and $W_0 = 1.31a$. The detailed description of the model can be found in [S43, S47].

$$\eta_r(z) = \frac{\beta(2Lg - 2H - W_0 - a)\ln(\frac{4L}{4H+2W_0+a})}{4L\ln(\frac{4L}{a}) - \beta(4Lg - 4H - 3a)\ln(\frac{4L}{4H+2a})} \tag{S2}$$

where H is the tip height above the sample and g corresponds to a fraction of the total induced charge. The n-th Fourier component needs to be included to account for the higher harmonic demodulation of α_{eff}. The final amplitude and phase contrast depend solely on the third order Fourier component of $\eta_r(z)$ because the far-field coefficients can be neglected here.

$$\frac{S_3}{S_3^{\text{ref}}} = \frac{\text{Abs}[(\eta_3)]}{\text{Abs}[(\eta_3^{\text{ref}})]} \tag{S3}$$

$$\Phi_3 - \Phi_3^{\text{ref}} = \text{Arg}[(\eta_3)] - \text{Arg}[(\eta_3^{\text{ref}})] \tag{S4}$$

Parameters of the FDM are summarized in Table I. We replace the electrostatic reflection coefficient β with a Fresnel reflection coefficient [S43] for a single dominant in-plane wave vector $k_{||} = 250000\ \text{cm}^{-1}$, comparable to the inverse of the expected tip radius of $\rho = 3.3{\cdot}10^5\ \text{cm}^{-1}$. To calculate the Fresnel coefficients for the stack, we use the transfer matrix method (TMM) for graphene layers with p-polarized light [S48]. In our model the tetralayer graphene is infinitesimal thin and a plane interface.

TABLE I. FDM Parameter

Name	Value
Demodulation order n	3
Tapping Amplitude H	60 nm
L [S47]	300 nm
g [S47]	$0.7e^{(i0.06)}$
Tip radius a	30 nm
SiO_2 thickness	90 nm

S3 s-SNOM Contrasts for different chemical potentials

In Figure S3 a) and c) the optical conductivity of the three stackings is plotted, calculated for a broadening of $\eta = 40$ meV and chemical potentials μ of 20 and 100 meV, respectively. In b) and d) same amplitude and phase data as in Figure 4 are plotted for ABCB referenced to ABAB. The calculated FDM spectra are shown for two different chemical potential. All three amplitude data sets show a higher peak at 0.38 eV, which can be either attributed to a smaller broadening or an increased chemical potential. For a change in the chemical potential, we expect a shift of the characteristic crossing of 1 and 0 in amplitude and phase, respectively. Furthermore, this also influences the contrast strength. A change in η would result in more pronounced features such as the peak in amplitude around 0.4 eV. For Flake 1 and Flake 2 the data fit better to 100 meV, especially the crossing of 1 in the amplitude is better reproduced. There are also indications for a smaller broadening, because amplitude data of Flake 1 indicate a sharper left flank and Flake 2 a more pronounced peak.

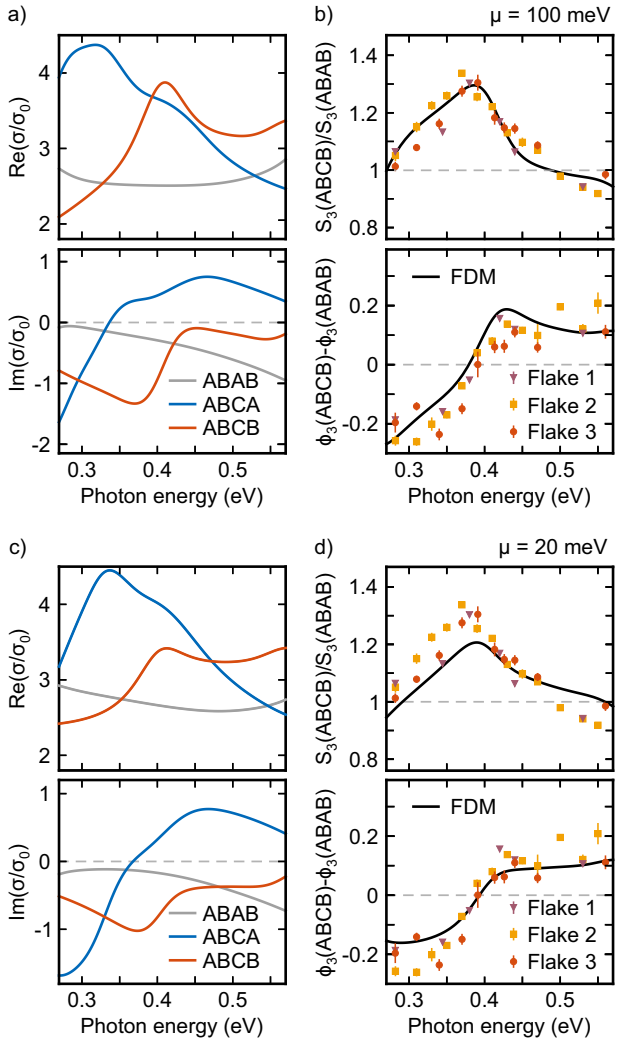

FIG. S3. Optical conductivity data for ABCB plotted for $\mu = 20$ meV a) and $\mu = 100$ meV c). Comparison between experimental data for the three flakes and the modelled calculation for the chemical potentials.

S4 Calculation of optical conductivity

For the calculation of the dynamic optical conductivity we employ the Kubo formula [S49]

$$\sigma(\omega)_{i,j} = \frac{e^2\hbar}{iS} \sum_{b_1,b_2,\boldsymbol{k}} \frac{n_f(e^{\boldsymbol{k}}_{b_1}) - n_f(e^{\boldsymbol{k}}_{b_2})}{e^{\boldsymbol{k}}_{b_1} - e^{\boldsymbol{k}}_{b_2}} \frac{\langle e^{\boldsymbol{k}}_{b_1} \,|\, \mathbf{v}_i \,|\, e^{\boldsymbol{k}}_{b_2}\rangle \langle e^{\boldsymbol{k}}_{b_2} \,|\, \mathbf{v}_j \,|\, e^{\boldsymbol{k}}_{b_1}\rangle}{\hbar\omega + e^{\boldsymbol{k}}_{b_1} - e^{\boldsymbol{k}}_{b_2} + i\eta}, \quad \text{(S5)}$$

where $e_b(\boldsymbol{k})$ are the eigenenergies of the Hamiltonian in band b at momentum point $\boldsymbol{k}$ and $|e^{\boldsymbol{k}}_b\rangle$ are the corresponding eigenvectors. The case of $e^{\boldsymbol{k}}_{b_1} = e^{\boldsymbol{k}}_{b_2}$ has to be considered separately and results in $\beta n_f(e^{\boldsymbol{k}}_{b_1})(n_f(e^{\boldsymbol{k}}_{b_1}) - 1)$. $\mathbf{v}_i(\boldsymbol{k})$ is the i-direction component of the velocity operator defined as $\mathbf{v}^n = \frac{i}{\hbar}[\mathbf{H}, \mathbf{x}^n]$ which can be expressed in the momentum-site basis as

$$\mathbf{v}^n_{o_1,o_2} = -\frac{i}{\hbar} \sum_{\boldsymbol{d}} e^{-i\boldsymbol{k}\boldsymbol{d}} H_{\boldsymbol{r}_1,\boldsymbol{r}_2+\boldsymbol{d}} \cdot (r^n_{o_1} - r^n_{o_2} + \boldsymbol{d}^n), \quad \text{(S6)}$$

with $\boldsymbol{r_i}$ a vector pointing to a site i in the lattice and $\boldsymbol{d}$ being a lattice vector. We chose the temperature to be room temperature (0.025 eV) and choose the broadening η as 40 meV. We chose a simple tight-binding Hamiltonian of the form

$$H = \sum_{i,j} \delta_{|\boldsymbol{r}_i - \boldsymbol{r}_j|, d_{cc}} \gamma_{\text{intra}} c^\dagger_i c_j + \delta_{|\boldsymbol{r}_i - \boldsymbol{r}_j|, d_{\text{layer}}} \gamma_{\text{inter}} c^\dagger_i c_j \quad \text{(S7)}$$

consisting of only nearest-neighbor intralayer (in a distance $d_{cc} = 1.42$ Å) and nearest-neighbor interlayer hopping (in a distance $d_{\text{layer}} = 3.35$ Å) with hopping energies of $\gamma_{\text{intra}} = 3.16$ eV and $\gamma_{\text{inter}} = 0.39$ eV. We shift the Fermi energy to 50 meV. The modeling parameters, Fermi-energy and broadening η were tweaked for the best agreement with the experimental results.

S5 Calculation of the tentative phase diagram

For the calculations of the tentative phase diagram we use a more sophisticated low energy model by adopting a Slonzecewski-Weiss-McClure (SWMC) Hamiltonian, with parameters chosen based on Ref. [S50] summarized in Table II. The Hamilton-matrix can now be constructed as

$$H^y_{i,j}(\boldsymbol{k}) = \delta_{i,j}\delta_{i,A}\Delta_y + \sum_{u_1,u_2\in\mathbb{Z}} \sum_n \delta_{d^{u_1,u_2}_{i,j},d_n} e^{-i\boldsymbol{k}\boldsymbol{R}(u_1,u_2)} \gamma_n\,, \quad \text{(S8)}$$

where i and j are site indices within the unit cell, y marks the type of the lattice and is either ABAB, ABCA or ABCB and $\delta_{i,A}$ is one if i is an A-site and 0 otherwise. u_1 and u_2 iterate over all unit cells in the infinite lattice, $\boldsymbol{R}(u_1, u_2)$ gives the vectorial distance between the unit cells and $d^{u_1,u_2}_{i,j}$ gives the distance between site i and the image of site j shifted by u_1 and u_2 unit-cell vectors.

The values for the Δ_y are chosen such that we roughly reproduce the low energy behavior of the bandstructures from Ref. [S12]. Therefore, the model is a good representation of the low energy degrees of freedom near half-filling. The low energy bands can be found in the main text Figure 1 a).

Random-phase approximation

To study the occurrence of magnetic and superconducting phases, we resort to the multi-orbital random-phase approximation that is based on the calculation of

TABLE II. SWMC model parameters

Name	Value in eV	Distance in Å
γ_0	2.553	1.42
γ_1	0.343	3.35
γ_2	−0.009	6.70
γ_3	0.18	4.16
γ_4	0.173	3.64
γ_5	0.018	6.85
Δ_{ABAB}	−0.003	0.0, A site
Δ_{ABCA}	0.0	0.0, A site
Δ_{ABCB}	−0.018	0.0, A site

an effective pairing interaction mediated by transverse and longitudinal spin-fluctuations. The central object in this approach is the particle-hole loop, which can be written as (the lower sign is for the particle-particle loop)

$$L_{o_1,o_2,o_3,o_4}(q) = \frac{1}{N}\sum_k G_{o_1,o_2}(k)G_{o_3,o_4}(q \pm k), \tag{S9}$$

where o_i are the site indices, $q \equiv (\omega_q, \boldsymbol{k})^T$ is the frequency-momentum four vector and $SU(2)$-invariance was exploited. Here, G is the Greens function defined by

$$G_{o_1,o_2}(k) = u_{o_1,b}(\boldsymbol{k})\frac{1}{i\omega_k - e_b(\boldsymbol{k})}u^*_{o_2,b}(\boldsymbol{k}), \tag{S10}$$

where $u_{o,b}$ denotes the orbial-to-band transformations. As initial interaction we assume an on-site Hubbard U. Here, wee only study the static limit $\omega_q \to 0$ as this limit contains most dominant fluctuations. Additionally, this choice of initial interaction restricts the orbital combinations in Eq. (S9) to $o_3 = o_2$ and $o_1 = o_4$. The Matsubara sum in Eq. (S9) can be performed analytically by the means of the contour integration technique, which results in the Lindhard formula for multi-orbital systems, cf. Eq. (S11).

$$L_{o_1,o_2}(\boldsymbol{q}) = \frac{1}{N}\sum_{b_1,b_2,\boldsymbol{k}} u_{o_1,b_1}(\boldsymbol{k})u^*_{o_2,b_1}(\boldsymbol{k})u_{o_2,b_2}(\boldsymbol{k}-\boldsymbol{q})u^*_{o_1,b_2}(\boldsymbol{k}-\boldsymbol{q})\frac{n_f\big(e_{b_1}(\boldsymbol{k})\big) - n_f\big(e_{b_2}(\boldsymbol{k}-\boldsymbol{q})\big)}{e_{b_1}(\boldsymbol{k}) - e_{b_2}(\boldsymbol{k}-\boldsymbol{q})} \tag{S11}$$

$$\begin{aligned} V^{s_1,s_2,s_3,s_4}_{o_1,o_2,o_3,o_4}(\boldsymbol{k},\boldsymbol{k}') = {} & U\delta^{s_1,s_3}_{o_1,o_2}\delta^{s_2,s_4}_{o_3,o_4}\delta^{s_1,\bar{s}_2}_{o_1,o_4} - U\delta^{s_1,s_4}_{o_1,o_2}\delta^{s_2,s_3}_{o_3,o_4}\delta^{s_1,\bar{s}_2}_{o_1,o_4} \\ & + \left[\frac{U^2L(\boldsymbol{k}+\boldsymbol{k}')}{1+UL(\boldsymbol{k}+\boldsymbol{k}')}\right]_{o_1,o_2}\delta^{s_1,s_4}_{o_1,o_4}\delta^{s_2,s_3}_{o_2,o_3} - \left[\frac{U^3L(\boldsymbol{k}-\boldsymbol{k}')^2}{1-U^2L(\boldsymbol{k}-\boldsymbol{k}')^2}\right]_{o_1,o_2}\delta^{s_1,s_3}_{o_1,o_3}\delta^{s_2,s_4}_{o_2,o_4}. \end{aligned} \tag{S12}$$

$$\Gamma^{\mathrm{S/T}}(\boldsymbol{k},\boldsymbol{k}',b,b') = \sum_{o_1,o_2,o_3,o_4} u^*_{o_1,b}(\boldsymbol{k})u^*_{o_2,b}(-\boldsymbol{k})V^{\mathrm{S/T}}_{o_1,o_2,o_3,o_4}(\boldsymbol{k},\boldsymbol{k}')u_{o_3,b}(\boldsymbol{k}')u_{o_4,b}(-\boldsymbol{k}'). \tag{S13}$$

$$\lambda_{\mathrm{SC}}\Delta(\boldsymbol{k},b) = \frac{1}{N}\sum_{\boldsymbol{k}'b'}\Gamma^{\mathrm{S/T}}(\boldsymbol{k},\boldsymbol{k}',b,b')\frac{n_f\big(e_{b'}(\boldsymbol{k}')\big) - n_f\big(-e_{b'}(-\boldsymbol{k}')\big)}{e_{b'}(\boldsymbol{k}') + e_{b'}(-\boldsymbol{k}')}\Delta(\boldsymbol{k}',b') \tag{S14}$$

For the calculations presented in Figure 1 in the manuscript we chose a momentum resolution of $N_{\boldsymbol{k}} = 24 \times 24$ for the transfer momentum $\boldsymbol{q}$ and further refine the inner momentum sum in Eq. (S11) on a $N_{\boldsymbol{k}_f} = 4800 \times 4800$ mesh to resolve the low-energy features around the valleys K and K'.

As the effective spin fluctuation vertex Eq. (S12) is proportional to $(1+UL)^{-1}$, we can directly access magnetic instabilities by diagonalizing the loop and searching for eigenvalues close to the Stoner condition, i.e. $\lambda \approx -1/U$. The corresponding eigenvector encodes the ordering type and the strength of the magnetization at each site, up to an unknown prefactor. To avoid numerical instabilities when calculating superconducting gap functions using the FLEX vertex, we perform the matrix inversions $1/(1+UL)$ and $1/(1-U^2L^2)$ in Eq. (S12) in the eigenspace of L and add a small imaginary broadening constant $i\,\eta_{\mathrm{FLEX}} = 0.1\,\mathrm{meV}$ to all the eigenvalues in the denominator. Note that the energy scale of this broadening constant is to be compared with (and has to be very small in regard to) the *vertex* energy scales, i.e. $\sim 5.1\,\mathrm{eV}$ and *not the flat band* energy scales.

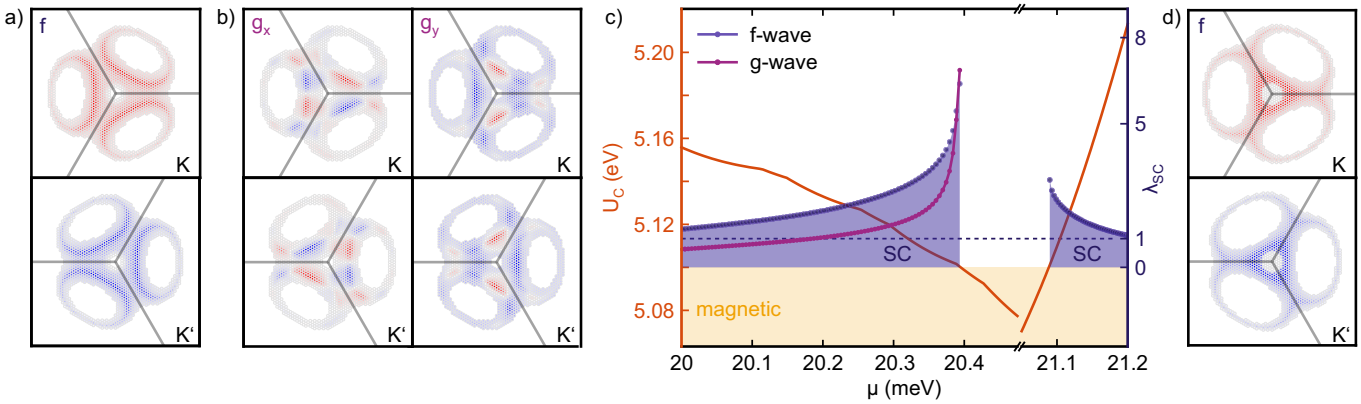

FIG. S4. **Tentative phase diagram of ABCB graphene.** a) Gap symmetry of the leading (f-wave) superconducting instability in the left region. The sign of the superconducting order parameter flips from valley K to K'. b) Subleading degenerate superconducting gap parameters in the left region. Left column: g_x-wave symmetric gap function in both valleys, right column: g_y-wave symmetric gap function. c) Constructed phase diagram from RPA and FLEX. We plot the critical RPA interaction strength U_c as a function of chemical potential μ. With $U = 5.1\,\mathrm{eV}$ we argue that for $20.4\,\mathrm{meV} \lesssim \mu \lesssim 21.1\,\mathrm{meV}$ the system is magnetically ordered. Superconducting regions emerge for $\mu \lesssim 20.4\,\mathrm{meV}$ (left region) and $\mu \gtrsim 21.1\,\mathrm{meV}$ (right region). The right (blue) y axis encodes the strength of the leading superconducting order parameter with λ_{SC} roughly corresponding to a normalized critical temperature of the superconducting phase transition. In the left region, the leading f-wave triplet amplitude [cf. a)] is competing with a subleading g-wave singlet amplitude [cf. b)]. In the right region, the singlet amplitude is minuscule and only the f-wave symmetric triplet gap is favored [cf. d)]. d) Gap symmetry of the leading (f-wave) superconducting instability in the right region. The sign of the superconducting order parameter flips from valley K to K'.

Linearized gap equation

Close to the magnetic phase transition, magnetic fluctuations can become substantially large and mediate an attractive pairing interaction between the electrons. Assuming that spin- and charge fluctuation provide the superconducting glue in the system, we confine our considerations to the vicinity of the Fermi surface and only treat scattering processes from state $(\boldsymbol{k}, -\boldsymbol{k})$ on Fermi surface $\mathcal{S}_b$ to state $(\boldsymbol{k}', -\boldsymbol{k}')$ on Fermi surface $\mathcal{S}_{b'}$. To this end, we project the pairing vertex Eq. (S12) from orbital to band space Eq. (S13) and solve the linearized gap equation Eq. (S14) in the singlet and triplet channel separately. The proper pairing vertex in each respective channel is obtained by (anti-) symmetrizing the orbital vertex function Eq. (S12) such that

$$V^{\mathrm{S/T}} = \frac{1}{2}\left[V^{s_1,s_2,s_3,s_4}_{o_1,o_2,o_3,o_4}(\boldsymbol{k},\boldsymbol{k}') \pm V^{s_1,s_2,s_4,s_3}_{o_1,o_2,o_4,o_3}(\boldsymbol{k},-\boldsymbol{k}')\right] . \tag{S15}$$

We then solve the linearized gap equation (cf. Figure S5) in order to obtain strength and pairing symmetry of the superconducting order parameter, which takes the form of a non-hermitian eigenvalue problem. The largest eigenvalue $\lambda_{\mathrm{SC}} > 0$ will lead to the highest transition temperature T_c and the corresponding eigenfunction $\Delta(\boldsymbol{k}, b)$ determines the symmetry of the gap, which can be classified according to the irreducible representations of the point group of the normal-state Hamiltonian. Here, a value of $\lambda_{\mathrm{SC}} > 1$ (blue dotted horizontal line in Fig. S4) indicates that the transition to the superconducting state.

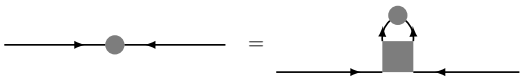

FIG. S5. Lowest order diagram for the pairing gap

Figure S4 comprises the low-energy phase diagram of ABCB graphene around $\mu \approx 20.7\,\mathrm{meV}$ calculated using the methods outlined above. Close to the conduction band magnetic instability, the emerging phases are presented in closer detail. As shown in panel c) we predict the system to order magnetically for values of μ where $U_c \leq 5.1\,\mathrm{eV}$ (orange line, left axis). Around the magnetic instability the possibility for superconducting order driven by magnetic fluctuations arises. The blue curve (right axis) shows the strength of the linearized gap equation eigenvalue λ_{SC} corresponding to an f-wave symmetric gap. Figures S4 a-b) display the symmetry of the leading [cf. a)] and competing, subleading [cf. b)] gap function for the left SC region. Remarkably the system prefers an f-wave symmetric spin triplet order parameter over a nodal, two-fold degenerate g-wave singlet order parameter. In panel c), we encode the strength of the g-wave singlet order parameter as green curve on the blue (right) axis. In the right region the triplet f-wave order shown in Figure S4 d) dominates clearly over any singlet order parameter found within our approach.

To conclude with the results presented in Figure S4, some technical subtleties need to be taken care of when calculating the magnetic RPA susceptibility, setting up the effective pairing vertex Eq. (S12) in fluctuation-exchange approximation, and solving the linearized gap equation Eq. (S14). Naïvely, one might think of refining the $\boldsymbol{k}'$ momentum sum in the particle-particle bubble Eq. (S14) in a similar manner as we presented for the $\boldsymbol{k}$ sum in the RPA Eq. (S11). However, employing such refinement may break point group symmetries present in the normal-state Hamiltonian, e.g. C_3 rotational symmetry around the z-axis. To conserve both degeneracy of multi-dimensional representations and the order of instabilities, we need to avoid any such tendency when solving the linarized gap equation Eq. (S14). The FLEX pairing vertex, though, is required to be set up on an adequate momentum mesh that captures the features of the Fermi surface. Therefore, we adjust the coarse mesh to the size of the fine mesh and finally resolve all quantities with $N_{\boldsymbol{k}} = 4800 \times 4800$. Unfortunately, keeping the full resolution in both $\boldsymbol{k}$ and $\boldsymbol{q}$ is numerically unfeasible. So we reduce numerical cost and restrict the particle-hole loop calculations to those transfer momenta $\boldsymbol{q}$ that connect two arbitrary points $\boldsymbol{k}_f$ and $\boldsymbol{k}'_f$ on the Fermi surface. The problem of setting up the FLEX vertex $V^{S/T}(\boldsymbol{k}_f, \boldsymbol{k}'_f)$ then reduces to determining proper points on the Fermi surface, i.e. momentum points that satisfy $|\epsilon_b(\boldsymbol{k}) - \mu| < \eta_{\mathrm{FS}}$. To treat this cutoff problem consistently, we choose a large cutoff of $\eta_{\mathrm{FS}} = 1\,\mathrm{meV}$ to assure that the Fermi surface broadening may not be smaller than thermal broadening in the system: $\eta_{\mathrm{FS}} > T$. The explicit contraction of the FLEX vertex with the particle-particle loop Eq. (S14) will suppress all contributions that are not in the immediate vicinity of the Fermi surface $\propto (2\epsilon)^{-1}$. Since the Fermi surface changes as we alter the chemical potential, we assure that for each dome presented in Figure 1 the Fermi surface is chosen such that $\epsilon_b(\boldsymbol{k}) \in [\mu_{\mathrm{min}} - \eta_{\mathrm{FS}}, \mu_{\mathrm{max}} + \eta_{\mathrm{FS}}]$, where μ_{min} (μ_{max}) denotes the minimal (maximal) chemical potential for which we want to resolve the superconducting instabilities.